Journal of Petroleum Science and Engineering 145 (2016) 256–265

Contents lists available at ScienceDirect

Journal of Petroleum Science and Engineering

journal homepage: www.elsevier.com/locate/petrol

Characterization of petrophysical properties using pore-network and lattice-Boltzmann modelling: Choice of method and image sub-volume size

Nayef Alyafei [a], Thomas J. Mckay [b], Theis I. Solling [c,*]

[a] Department of Petroleum Engineering, Texas A&M University at Qatar, Qatar
[b] Maersk Oil Research Technology Centre, Qatar
[c] Department of Chemistry, University of Copenhagen, Denmark

ARTICLE INFO

Article history:
Received 13 January 2016
Received in revised form
17 May 2016
Accepted 20 May 2016
Available online 20 May 2016

Keywords:
CT scanning
Digital rock physics
Pore network modelling
Lattice-boltzmann

ABSTRACT

The invention and progression of micro-CT scanning technology has significantly improved the quality and resolution of tomographic images. It is now possible to fully resolve simpler pore systems and thus perform static modelling of flow properties. A substantial amount of research has been performed to fully develop workflows relating to the analysis of a number of sandstone and carbonate core samples from benchmark outcrop rocks. In this study the focus is on Bentheimer, Clashach and Doddington sandstone rocks and on Estaillades, Ketton and Portland limestone samples. These benchmarks have been imaged using a micro-CT at a resolution of about 3 μm.

The image-based modelling and analysis of the absolute permeabilities gave values within a similar range of the experimental results for all three of the sandstone samples. Results deviated greatly for the limestone due to the presence of unresolvable pore space, reflecting the need to acquire higher resolution data to obtain a full digital description of the samples at hand. The variation in the petrophysical parameters with the size of the selected subvolume (either 512 or 1024 voxels) is the focus in the present study. With the notable exception of Clashach, the homogeneous sandstones do give the same results for the two subset sizes. The limestone data varies by more than a factor of four for the permeabilities whereas the porosity varies by less than a factor of two. The extracted pore size distributions vary quite significantly from the experimental ones regardless of the subset size and the bimodal nature of the limestone pore space is not captured at all. This is reflected in the capillary pressure curves, the image-based ones are significantly different from the experimental ones. The reconstructed 3D acquisitions and 2D slices will be posted online to form a database that allows for download of the tomographic images and extracted pore spaces to serve as a resource for future comparative modelling studies.

© 2016 Elsevier B.V. All rights reserved.

1. Introduction

An understanding of the mechanisms that govern fluid flow in porous media is of great importance when addressing the productivity of conventional oil reservoirs. A key aspect is the spatial arrangement of the pore spaces and pore throats. Such information can be gathered in CT scanning experiments and the outcome has become more reliable with the advent of in-house instruments, where the resolution is in the μm and even nm regime (Wildenschild and Sheppard, 2013). The result is a digital 3D description of the core which can subsequently be used for modelling of central petrophysical parameters such as porosity and permeability as well as more advanced two-phase flow properties (Arns et al., 2002; Blunt et al., 2012; Valvatne and Blunt, 2004). It is also possible conduct simulations to obtain three-phase flow parameters that are otherwise very difficult to obtain (Alizadeh and Piri, 2014; Suicmez et al., 2007; Fenwick and Blunt, 1998). The technique is non-destructive, meaning that further analysis can be conducted on the same core once the 3D imaging and reconstruction is completed. This is particularly important when further lab studies need to be conducted on the same piece of core.

Tomography can produce reliable images for samples with larger features, whereas samples with smaller features such as limestones are more challenging because the pore space often cannot be properly resolved. There are often large discrepancies between the results of laboratory measurements and image-based petrophysical data because of the difficulty in modelling the flow behavior through poorly resolved sections of the rock matrix (Marquez et al., 2013). Fig. 1 depicts a typical sandstone tomogram

* Corresponding author.

http://dx.doi.org/10.1016/j.petrol.2016.05.021
0920-4105/© 2016 Elsevier B.V. All rights reserved.

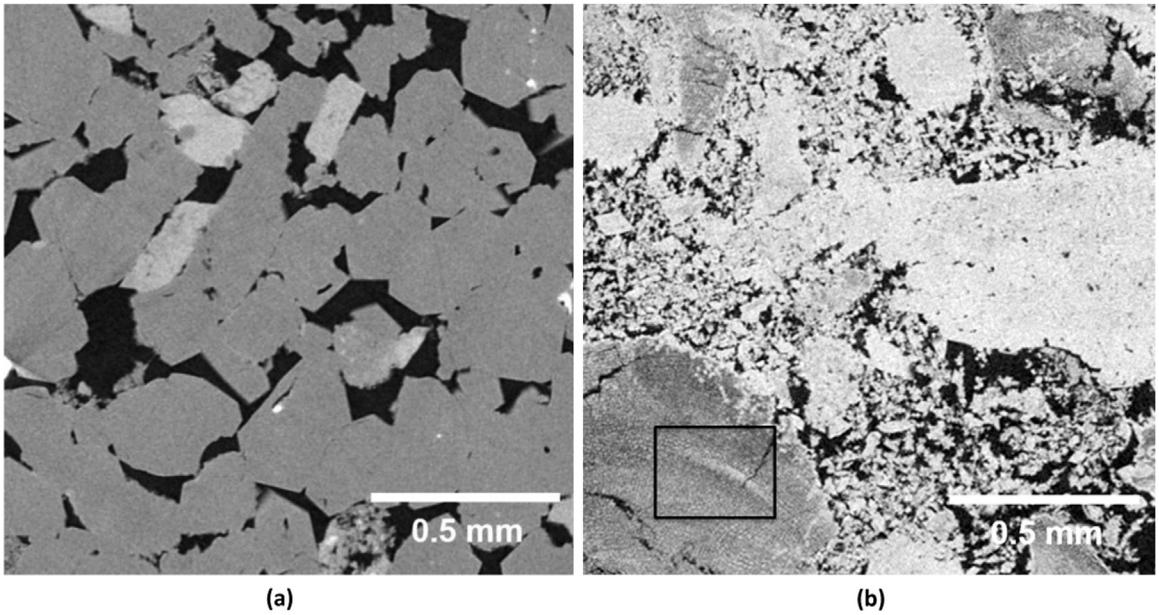

Fig. 1. a and 1b. A slice of a reconstructed tomogram from a (a) sandstone and (b) micritic carbonate showing the difference in size and complexity of the pore system, the box is indicating an area that is not properly resolved.

slice next to the one of a limestone, it can be seen that there are large sections in the image where it is not clear whether the area represents pore or grain.

The modelling of flow through a pore space like that of Fig. 1 (b) is likely to fail due to its complexity. When the rock in question is noticeably heterogeneous an additional challenge arises in the sense that a volume has to be chosen for the modelling that represents the entire sample; a so-called representative volume (REV) (Sok et al., 2010; Wilke et al., 2003).

The way that the computational time varies with the subset size depends significantly on the method in question and on how efficient the code has been written (Biferale et al., 2013). When the focus is on the modelling of flow within the framework of either percolation theory or attempts to solve the Naiver-Stokes equations using lattice-Boltzmann theory one relies on the implementations of the Blunt (Blunt et al., 2002; Dong and Blunt, 2009) and Arns (Arns et al., 2001; Arns et al., 2004) groups, respectively. The Blunt code is distributed free of charge whereas the code of the Arns group is proprietary software which can be obtained on a commercial basis. It is essential to be quite precise when deciding on the subset to be used in the modelling, particularly in the case of the lattice-Boltzman based methods because this method is computationally quite intensive. In the present work we set out to test the digital sampling size (512^3 vs 1024^3) and the performance of percolation theory vs a lattice-Boltzmann approach as implemented in the codes from the Blunt and the Arns groups. The variation in subset size will address how the presence of microporous regions and general sample heterogeneity influences the result. For fully resolved systems such as large grain clastics, the results should be minimally dependent on subset size in almost all cases, whereas limestones would be expected to require larger REVs to represent the structure. Each of the core samples was experimentally tested after it was scanned in three dimensions to ensure that the experimental porosities and absolute permeabilities were obtained from the sample that was actually scanned.

The samples that are in focus presently can be regarded as industry standards and their properties have been the topic of a wide variety of studies (Andrew et al., 2014; Alyafei et al., 2015; Turner et al., 2004). Thus, the results in this work can be compared to other 3D modelling initiatives to serve as an additional reference in establishing tomography as a reliable technique.

The main purpose of the present work is to assess the impact of changing the image volume from 512^3 to 1024^3 on a range of different image-derived parameters. The study also enables us to address the performance of two different publicly available packages for the generation of petrophysical parameters to communicate the potential challenges and recommendations. This encompasses issues pertaining to the methods that are employed in pore network generation and the consequences for the image-based predictions.

2. Experimental and computational methodologies

2.1. Rock samples and experimental characterization

A total of six samples were studied in this paper: three sandstones and three carbonates. The three sandstones studied were Bentheimer, Clashach, and Doddington. Bentheimer originates from Germany and is generally composed of 97.5% quartz, 2% feldspar, and 0.5% kaolinite (Dubelaar and Nijland, 2015). Clashach comes from the UK and usually consists of about 90% quartz and 10% feldspars (Ngwenya et al., 1995). Doddington comes from the UK and is composed of 95.2% quartz and 4.8% white micas and feldspars (Santarelli and Brown, 1989).

The three limestones studied were Estaillades, Ketton, and Portland. Estaillades comes from France and consists of 99% calcite along with 1% dolomite and silica (Watson, 1911). Ketton comes from the UK and comprises of 99.1% calcite and 0.9% quartz (Andrew et al., 2014). Portland comes from the UK and consists of 96.6% calcite and 3.4% quartz (Brenchly and Rawson, 2006). The porosity and permeability were measured on the same samples of 10 mm in length at the Imperial College London. The porosity was measured using the volume balance method were a comparison between the dry and the full saturated sample is taken into account. The permeability was measured using a custom made Hassler cell with cylindrical confining pressure, the cell was made

Table 1.
Scanning parameters for the six samples.

Sample	Bentheimer	Clashach	Doddington	Estaillades	Ketton	Portland
Type	Sandstone	Sandstone	Sandstone	Limestone	Limestone	Limestone
Locality	Germany	United Kingdom	United Kingdom	France	United Kingdom	United Kingdom
Voxel Size	2.95 μm	3.21 μm	2.85 μm	2.82 μm	2.77 μm	2.88 μm
Scan Height	7.5 mm	9.0 mm	8.0 mm	6.5 mm	8.0 mm	7.0 mm
Scan type	Double helix					
Voltage	80 kV					
Current	100 μA					

Table 2.
Segmentation Parameters for each rock based on their mineralogy.

Sample	Bentheimer	Clashach	Doddington	Estaillades	Ketton	Portland
Lower threshold	10,800	11,140	10,620	11,240	13,260	12,900
Upper threshold	10,880	11,240	10,685	11,360	13,350	13,120

to fit samples of ≈ 5 mm in diameter and up to 25 mm in length. Two pumps (Teledyne pump, ISCO 1000D) were used, one for water injection and one for applying confining pressure. Mercury injection capillary pressure (MICP) experimentswere conducted using an Autopore, IV 9520 at Weatherford Laboratories, East Grinstead, UK.

2.2. Micro-CT imaging

Tomographic datasets were obtained and analysed using the micro-CT scanner built at the Australian National University (ANU) and housed at the newly established digital core laboratory at Maersk Oil Research and Technology Centre (MORTC), Qatar. The scans were conducted on a 4.8 mm plug of each rock with an image resolution of about 3 μm. The plugs were mounted in an anodized aluminum sample holder with an inner diameter of 5 mm. The holder was scanned with an aluminum-filtered (3 mm) polychromatic X-ray source (Nanofocus, GE), operated at 80 kV and 100 μA. Radiographs (2048 × 2048 pixel^2) were captured by a flat panel detector (Varian). The scans were performed in which 2520 projections were acquired over the helical pitch (all double helix scans), at a source-camera distance of 354 mm. A list of the experiments is shown below in Table 1.

2.3. Image processing: segmentation and subvolume extraction

A number of programs were used for the image processing. MANGO (Medial Axis and Network GeneratiOn), is a program developed at the Australian National University which can binarise and analyse the greyscale data (Sakellariou et al., 2007). MORPHY is a scripting program, which was designed at the University of New South Wales (UNSW) and can be used to digitally determine the absolute permeability of a segmented data set along with other petrophysical information within the lattice-Boltzmann framework (Arns et al., 2001; Arns et al., 2004). As an alternative approach, the Blunt group has driven the development of using percolation theory on a pore network to obtain petro physical parameters (Blunt et al., 2002; Dong and Blunt, 2009). Network extraction is the first step; a maximal ball algorithm is used to extract topologically representative networks from the images. The method finds the largest spheres that fit in the pore space, while chains of smaller spheres connecting them represent throats. Details of the method are provided elsewhere, (Dong and Blunt, 2009). Subsequently, fluids are percolated through the network to obtain a model of the flow properties (Blunt et al., 2002; Dong and Blunt, 2009). The Drishti program developed at the ANU, was used to make the images of the 3D models from the network and segmentation output of the MANGO software (Ribi et al., 2008). The 2D projection data that was acquired on the Heliscan micro-CT was reconstructed into a 3D volume using the mango software package. Most of the image processing in this paper requires the use of a supercomputer, the one that is employed presently consists of six E5-2697 CPUs in conjunction with six NVIDIA K10 GPUs and 48 16 GB RAM chips. The reconstructed image was cropped to a base of 1024^3 voxels and then segmented into two phases. One phase represents pore and the other a combination of solid grain, clays and porosity features smaller than one voxel. All of the samples were given different parameters for the segmentation based on their mineralogy (Table 2). The 1024^3 voxel images were cropped to the central 512^3 voxels in order to study the effect of sub-volume on the prediction of petrophysical properties. Two different methods were employed for determining the permeabilities: (1) A simulation based on the networks to calculate the single-phase permeability. The computation essentially treats the porous medium as a random resistor network with semi-analytically computed permeabilities for each element (Valvatne and Blunt, 2004). (2) The absolute permeability calculations were performed on the segmented data file (MORPHY) using a lattice-Boltzmann approach (Bernaschi et al., 2010). A Euclidean distance filter was then applied to the segmented files. The Euclidean distance is a filter that determines the minimum distance to a phase boundary and stores that information as a greyscale colour (Jones et al., 2009).

Fig. 2 shows an example of the subsetting and segmentation. The segmentation thresholds that are given in Table 2 are determined by manually assessing when a phase is grain or pore. This is obviously associated with some personal bias and constitutes a source of error. This is why we report the employed thresholds in Table 2. Manual segmentation is the only real option as reliable auto segmentation algorithms has yet to be developed. All the segmented 1024^3 voxel images used in this study are available for download at https://pete.qatar.tamu.edu/Research/imagingandmodelling/Documents/Segmented%20Images.zip.

3. Results and discussion

3.1. Experimental rock characterization

Fig. 3 shows slices (two-dimensional sections) of three-dimensional X-ray scans for all the rocks. The sandstone samples

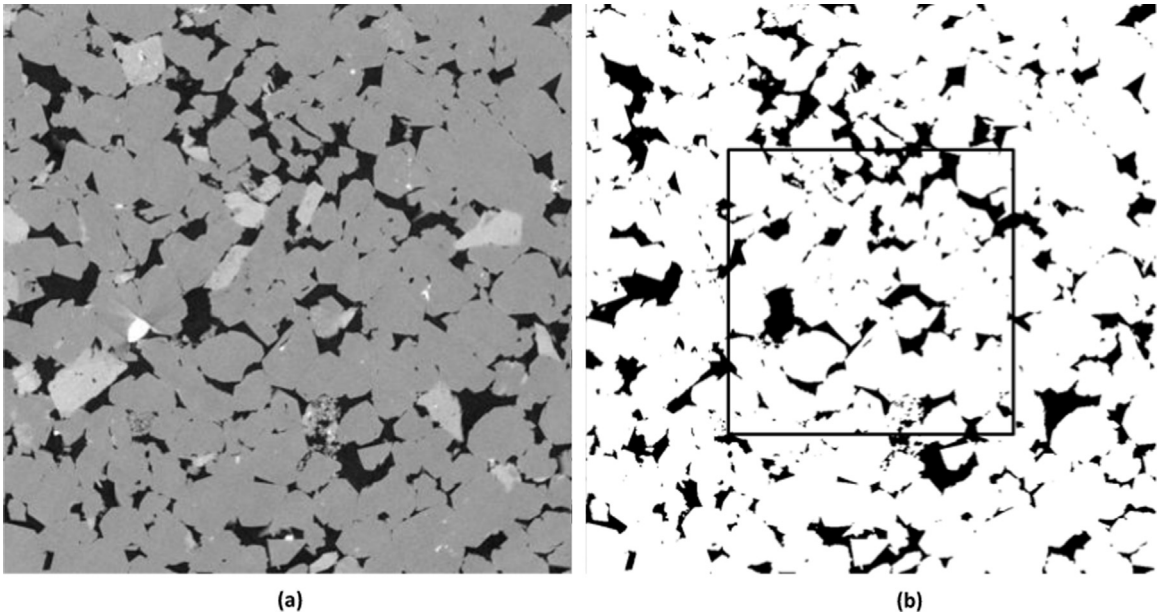

Fig. 2. a and 2b.(a) 2D grey scale cross section of Clashach sandstone cropped to the base of 1024×1024 pixel^2 and (b) the segmented image of (a). The black square at the center shows the cropped sub-section of 512×512 pixel^2.

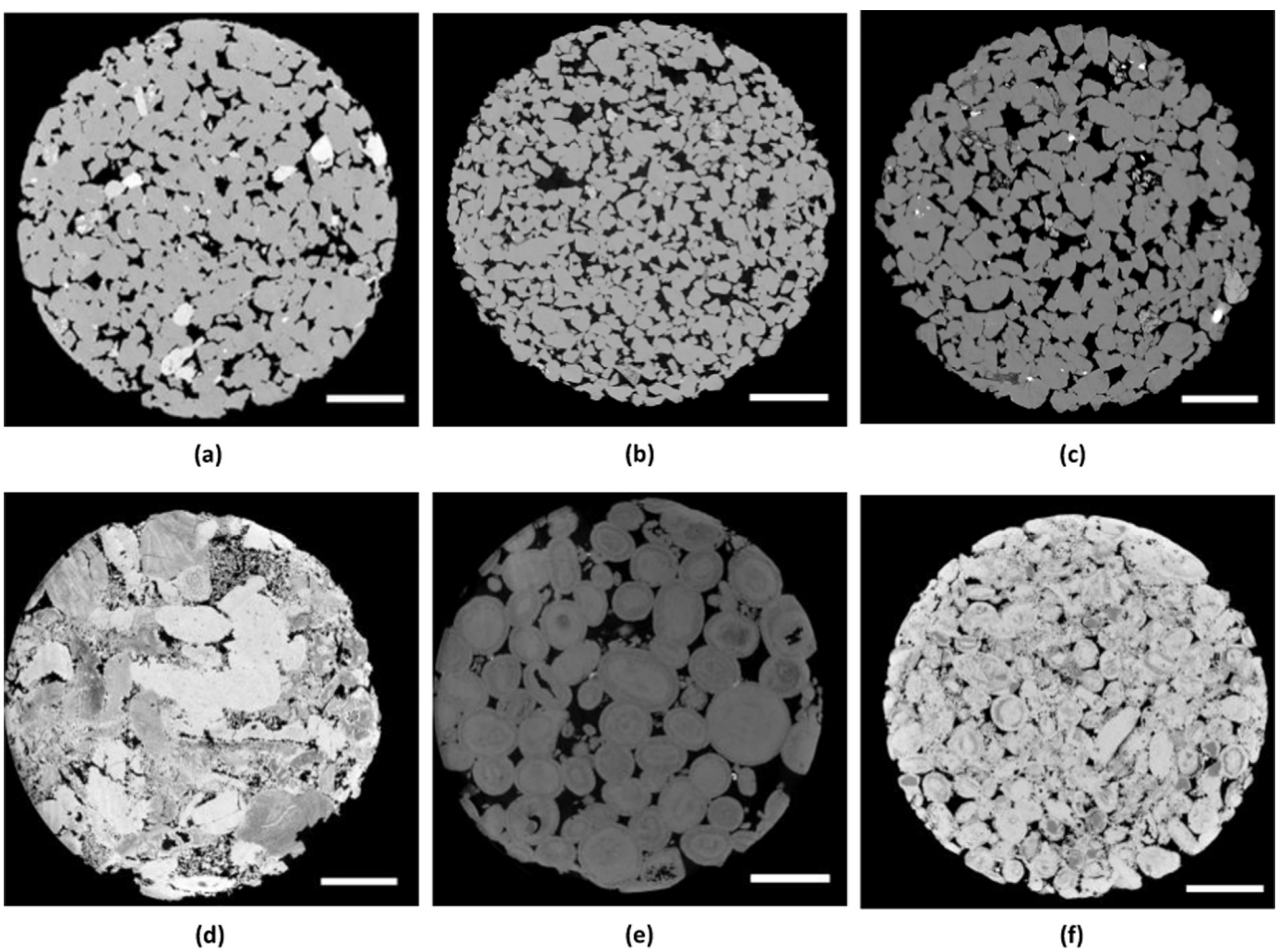

Fig. 3. (a–f). Grey scale micro-CT image cross-section for (a) Bentheimer, (b) Clashach, (c) Doddington, (d) Estaillades, (e) Ketton, and (f) Portland. The scale bar represents 1 mm.

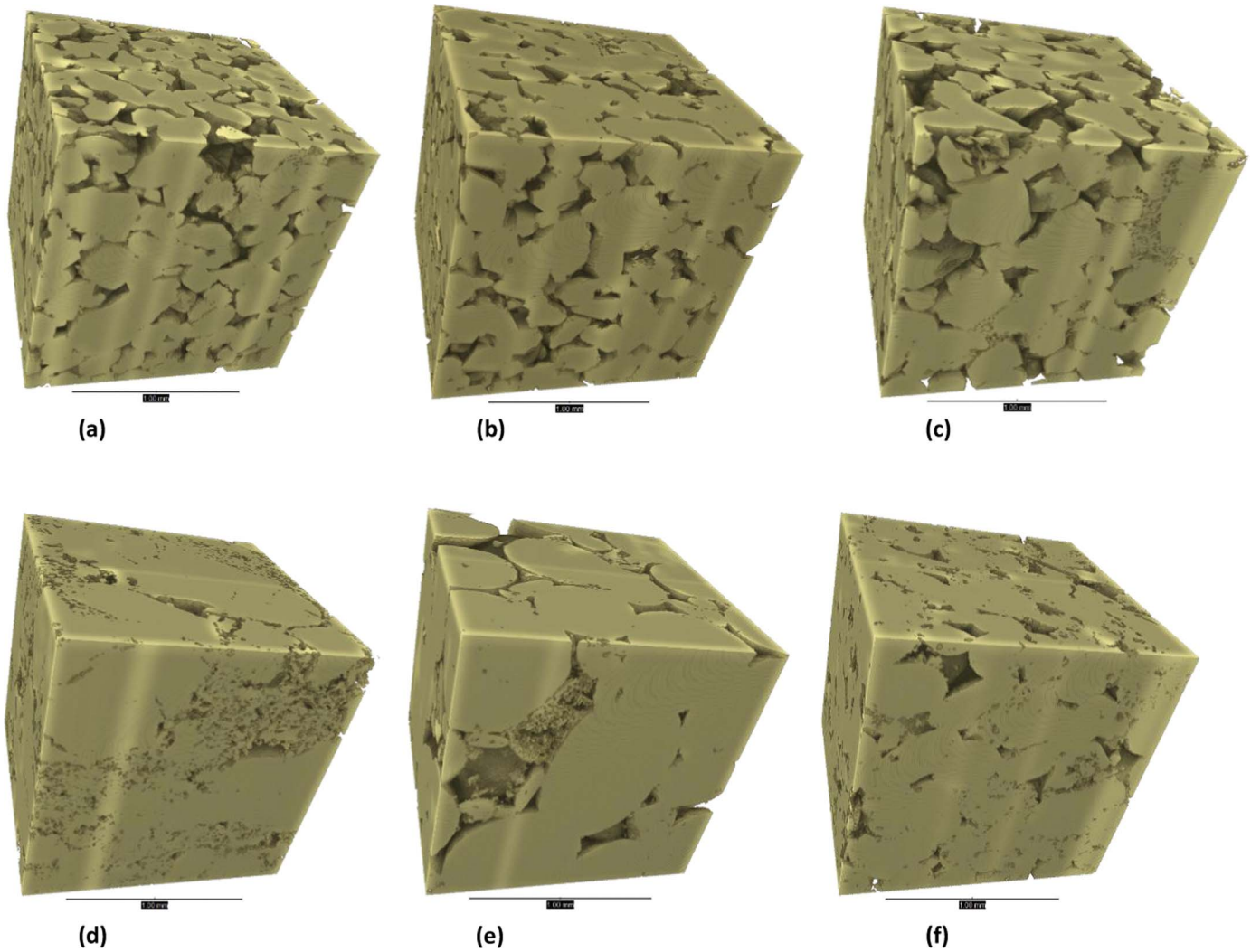

Fig. 4. (a–f): Segmented three-dimensional images of 512^3 voxels of (a) Bentheimer, (b) Clashach, (c) Doddington, (d) Estaillades, (e) Ketton, and (f) Portland.

(top row) have mostly homogeneous and resolved pore spaces, whereas the limestone samples (bottom row) have more complex and partially resolved pore spaces. Of the limestone samples Ketton seems to be the one which is most well behaved from a resolution and heterogeneity perspective. The 3D subsets of 512^3 voxels are shown in Fig. 4.

The MICP curves (Fig. 5) are further interpreted as by defining a pore entry radius, r_p:

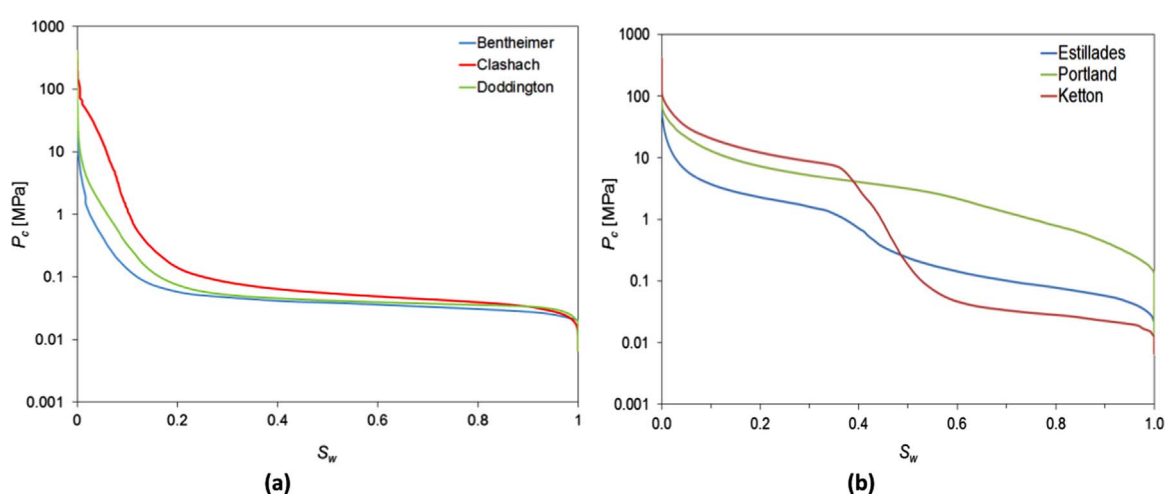

Fig. 5. a and 5b. Measured capillary pressure (mercury/air) as a function of equivalent water saturation for (a) the sandstone, and (b) limestone rocks used in this study.

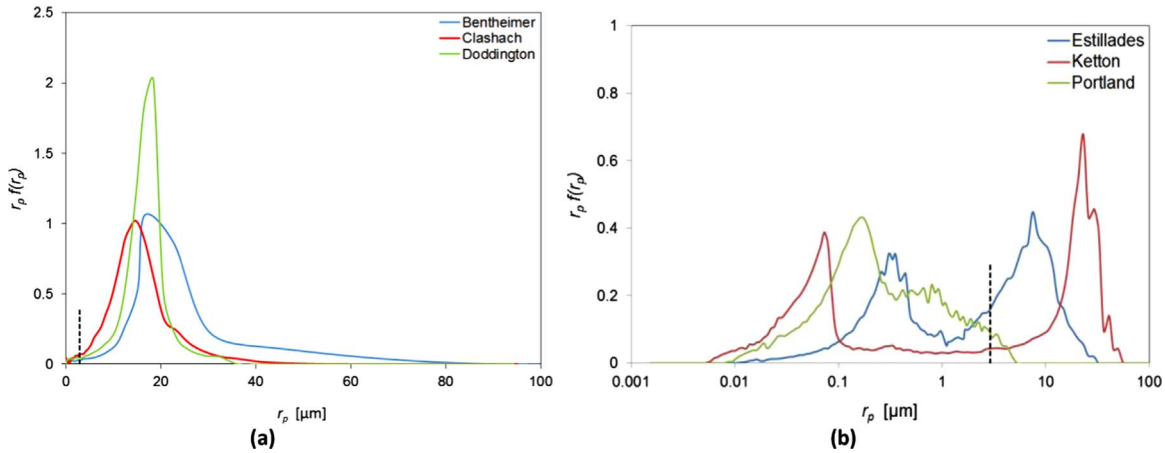

Fig. 6. a and 6b. The pore size distribution against pore throat radius for (a) the sandstone, and (b) limestone rocks used in this study. The dashed line depicts r_p=2.9 μm.

$$\frac{2\sigma\cos\theta}{P_c(S_w)}$$

Where P_c is capillary pressure [Pa], σ is interfacial tension, 0.48 N/m for a mercury/air system, θ is contact angle, 40°, S_w is water saturation.

Then, probability distribution function (f) of r_p can be achieved using the following equation (Dullien, 1992):

$$r_p f(r_p) = r_p \frac{dS_w}{dr_p} = -P_c \frac{dS_w}{dP_c} = -\frac{dS_w}{dlnP_c}$$

Fig. 6 shows the pore size distribution for all the rocks, the black dashed vertical line shows r_p of 2.9 μm which is our imaging resolution. Most of the sandstone pores are larger than the image resolution and should be visible in a CT experiment whereas the reverse applies for the limestone.

Table 3 shows a summary of the petrophysical data from the experimental MICP, porosity and permeability measurements on the small cores.

3.2. Image based results: pore-and throat-size distribution comparison between 512^3, 1024^3 and experimental values

Fig. 7 shows the extracted topological networks from the 512^3 voxel 3D images. Table 4 shows the network properties of the rocks at both subset sizes. Estaillades has the highest number of pores while Clashach has the lowest, this finding is consistent for both subset sizes. For the throats, the ordering is the same as for the pores in the case of the 512^3subset, however, for the 1024^3 set the ordering is swapped, it is Clashach that has the lowest number of throats. Consistently, Ketton has a significantly higher coordination number in the 1024^3 case whereas Clashach has the same coordination number for both subset sizes. Clashach has the largest average pore and throat radii and it can be seen that the trend amongst the pore and throat sizes are consistent in between the two different subsets. It is noteworthy that even for as homogenous a case as Doddington there is a roughly 40% discrepancy in going from 512^3 to 1024^3, the 1024^3values are always largest so the discrepancy could be a result of the 512^3 set being too small to capture enough large pores or that the 512^3 subset size fortuitously makes the choice of subset center location a bad one in the sense that it does not embrace a representative volume.

The computed throat radii distribution functions from the extracted networks are shown in Fig. 8 together with those derived from the MICP experiments. Note that our experimental resolution does not capture sub voxel porosity and hence we cannot definitively resolve or account for elements smaller than a few μm in size. Thus, it will be impossible to obtain good agreement with the experimental results for the limestone samples as a higher resolution is required. This finding is independent of the subset size. The image derived distribution function is uni-modal whereas the one derived from the MICP measurements is bimodal. This lack of quantitative agreement is of course also rooted in the limited experimental resolution. In this study, both the sandstone and carbonate rocks peak at the image resolution of 2.9 μm with insignificant variation between all the curves from PNM. Moreover, the results from Alyafei et al., 2013 and 2015 also showed the same behavior where the throat size distribution peaks around the image resolution regardless of the rock type with the same unimodal distribution. This seems to be a feature of maximal algorithm that needs to be tackled and outside the scope of this paper. The findings (Fig. 8) for the sandstone samples are also ambiguous and the 512^3 and 1024^3 results are virtually identical. Both the experimental and the image derived distribution functions are unimodal for the sandstone samples and this is independent of the subset size. The difference between the experimental and the theoretical results are significant, not only do they peak in different positions but their width also differs. The shape of the sandstone distribution functions do seem to be similar, the modelling does capture the tails of the Bentheimer, Clashach and Doddington distribution functions. For unknown reasons the PNM functions

Table 3.
Petrophysical properties of the rocks used in this study. Subscripts E and Hg denote poro-perm and MICP experiment, respectively.

Sample	Bentheimer	Clashach	Doddington	Estaillades	Ketton	Portland
Type	Sandstone	Sandstone	Sandstone	Limestone	Limestone	Limestone
Locality	Germany	UK	UK	France	UK	UK
ϕ_E	0.203	0.167	0.214	0.280	0.220	0.194
k_E [m^2]	1.19×10^{-12}	2.87×10^{-13}	1.03×10^{-12}	9.62×10^{-14}	2.18×10^{-12}	6.22×10^{-15}
ϕ_{Hg}	0.256	0.137	0.192	0.277	0.208	0.166
K_{Hg} [m^2]	1.21×10^{-12}	3.17×10^{-13}	1.04×10^{-12}	1.49×10^{-13}	6.35×10^{-13}	9.93×10^{-16}

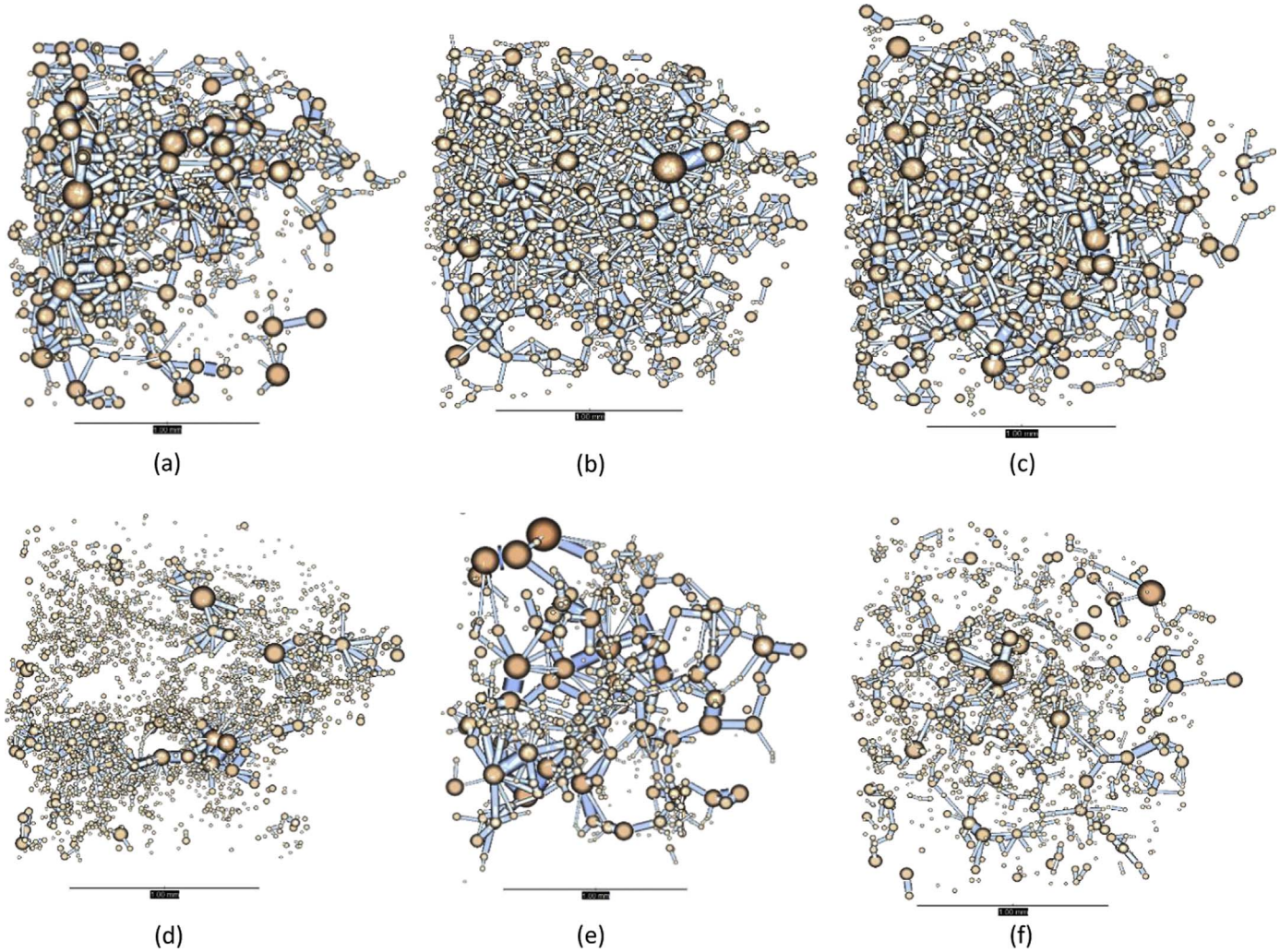

Fig. 7. (a–f): Three-dimensional pore and throat images (generated from the network extraction code Dong and Blunt (2009) for (a) Bentheimer, (b) Clashach, (c) Doddington, (d) Estaillades, (e) Ketton, and (f) Portland.

are compressed compared to the experimentally determined ones. So there does seem to be some impact of subset size for the numerical representation in the Table even with implication for the trends of the values in some cases. For the distribution functions the subset size does not seem to have much impact visually. However, the agreement with experimental values is quite poor. This is likely due to the way the PNM assigns pore boundaries, it is probably splitting up boundaries within the pore systems themselves. This combined with the inability to resolve some edges of the sandstone samples will likely lead to the left-shifted distributions seen here.

3.3. Comparison between image-based and experimental porosity and permeability

The porosity is obtained from the image by dividing the pore volume in the segmented image by the total volume. The results are shown in Table 5 for both subset sizes and compared to the

Table 4.
Statistical properties of the extracted pore networks from the Blunt Code.

512 Samples	Bentheimer	Clashach	Doddington	Estaillades	Ketton	Portland
Number of Pores	5084	3884	13,131	18,337	4003	12,534
Number of Throats	8154	5030	23,013	25,549	6213	8944
Average Pore Radius [μm]	7.94	9.44	4.30	4.15	7.43	4.31
Average Throat Radius [μm]	4.51	5.75	2.40	2.31	4.35	2.55
Average Coordination number	3.1	2.5	3.5	2.8	2.4	1.4
1024 Samples	Bentheimer	Clashach	Doddington	Estaillades	Ketton	Portland
Number of Pores	53,895	31,338	75,780	165,738	29,311	93,261
Number of Throats	90,438	37,709	146,516	238,571	46,811	66,646
Average Pore Radius [μm]	8.86	8.86	6.94	4.03	7.35	4.35
Average Throat Radius [μm]	5.18	5.29	3.81	2.25	4.34	2.59
Average Coordination number	3.3	2.4	3.8	2.9	3.2	1.4

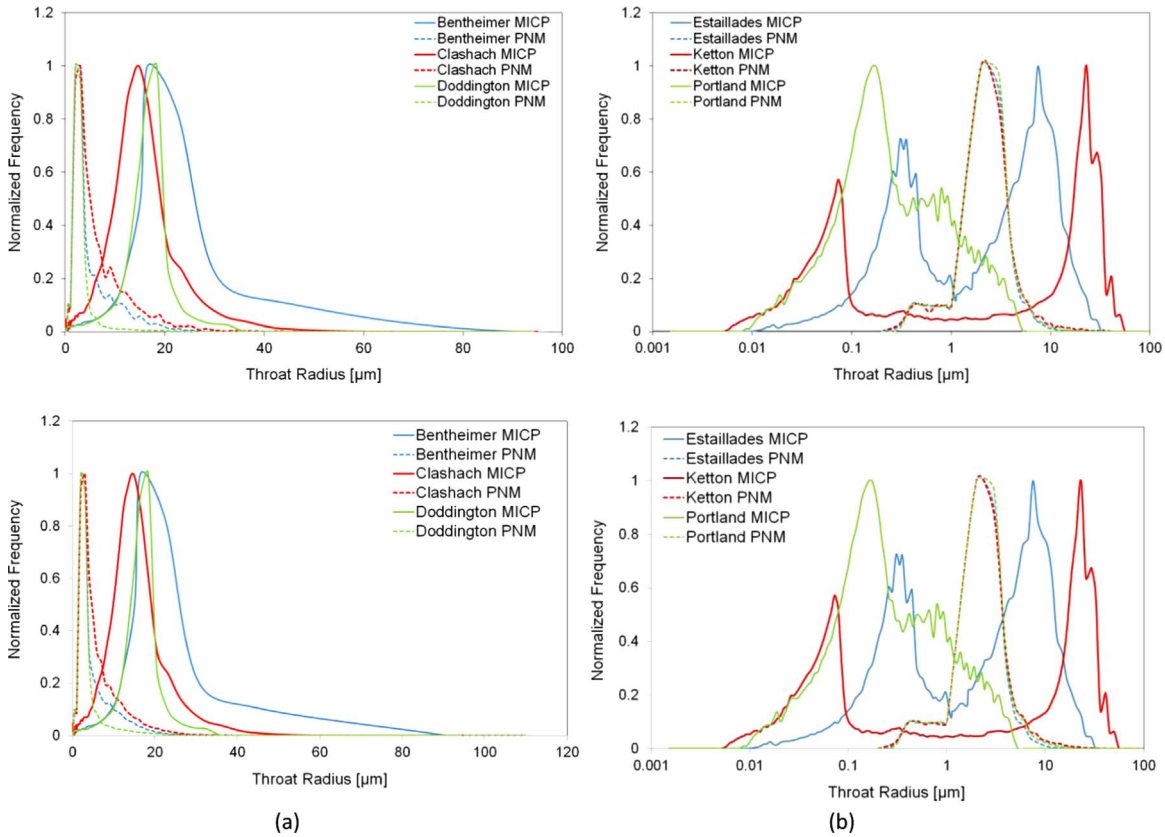

Fig. 8. Throat radius distribution from the extracted networks (top 512^3 and bottom 1024^3) compared to the MICP pore throat size distribution for (a) the sandstone and (b) the limestone rocks.

Table 5.
Summary of image porosity for the 512^3 and 1024^3 voxel images compared to the experimental values. The values were extracted using MANGO and the Blunt code. The same images were used for both analysis hence the porosities were identical, this was confirmed using both programs.

Sample	Bentheimer	Clashach	Doddington	Estaillades	Ketton	Portland
512^3 voxel ϕ_I	0.181	0.155	0.183	0.100	0.110	0.070
1024^3 voxel ϕ_I	0.186	0.136	0.207	0.102	0.124	0.077
ϕ_E	0.203	0.167	0.214	0.280	0.220	0.194

experimental values. The impact of subset size on porosity is small and the trend remains the same across the two subset sizes. The agreement with experimental values the board of samples is reasonable for the sandstones, with the image-based porosities reproducing the experimental trend. There is a significant discrepancy when it comes to the limestone samples and the experimental trend is not reproduced. The reason for this is the limited resolution in micro-CT experiments and thus the amount of unresolved porespace will determine the discrepancy between the experimental and image based values. This discrepancy is an indication of the amount of unresolved porosity. For example, in one of these experiments micro-CT images captured approximately 0.180/0.203 = 88% of the porosity of the Bentheimer sandstone sample which means that the amount of unresolved porosity is roughly 12%. For the Ketton limestone, the unresolved pores constitute the smallest fraction of the three limestone samples but it is still at 44%, i.e., half of the porosity for the limestone samples are not resolved. The amount of unresolved porosity found is not uncommon for carbonates when scanned at this resolution (Marquez et al., 2013). A good way to quantify the sub resolution porosity is to perform wet dry imaging on the samples and then quantify the partially filled pores using the difference between the two images (Sheppard et al., 2014).

The results of the image based permeability prediction within the framework of pore-network and lattice-Boltzmann modelling, on the two subset sizes are shown in Table 6. There is a distinct variation between the subset sizes, particularly for Clashach and the limestones. The values, however, stay roughly within the same order of magnitude of each other and of the experiment. The general trend in permeabilities was identical for samples in the

Table 6.
Summary of predicted permeability for the 512^3 and 1024^3 voxel images using PNM and LB compared to the experimental values.

Sample	Bentheimer	Clashach	Doddington	Estaillades	Ketton	Portland
512^3 voxel PNM k [m^2]	1.29×10^{-12}	1.23×10^{-12}	2.28×10^{-12}	1.68×10^{-13}	7.32×10^{-13}	1.02×10^{-15}
1024^3 voxel PNM k [m^2]	1.30×10^{-12}	6.87×10^{-13}	2.77×10^{-12}	2.63×10^{-14}	1.63×10^{-12}	3.90×10^{-15}
512^3 voxel LB k [m^2]	1.45×10^{-12}	1.26×10^{-12}	1.58×10^{-12}	9.33×10^{-14}	1.23×10^{-12}	1.23×10^{-14}
1024^3 voxel LB k [m^2]	1.48×10^{-12}	6.99×10^{-13}	2.58×10^{-12}	5.28×10^{-14}	2.24×10^{-12}	2.30×10^{-14}
k_E [m^2]	1.19×10^{-12}	2.87×10^{-13}	1.03×10^{-12}	9.62×10^{-14}	2.18×10^{-12}	6.22×10^{-15}

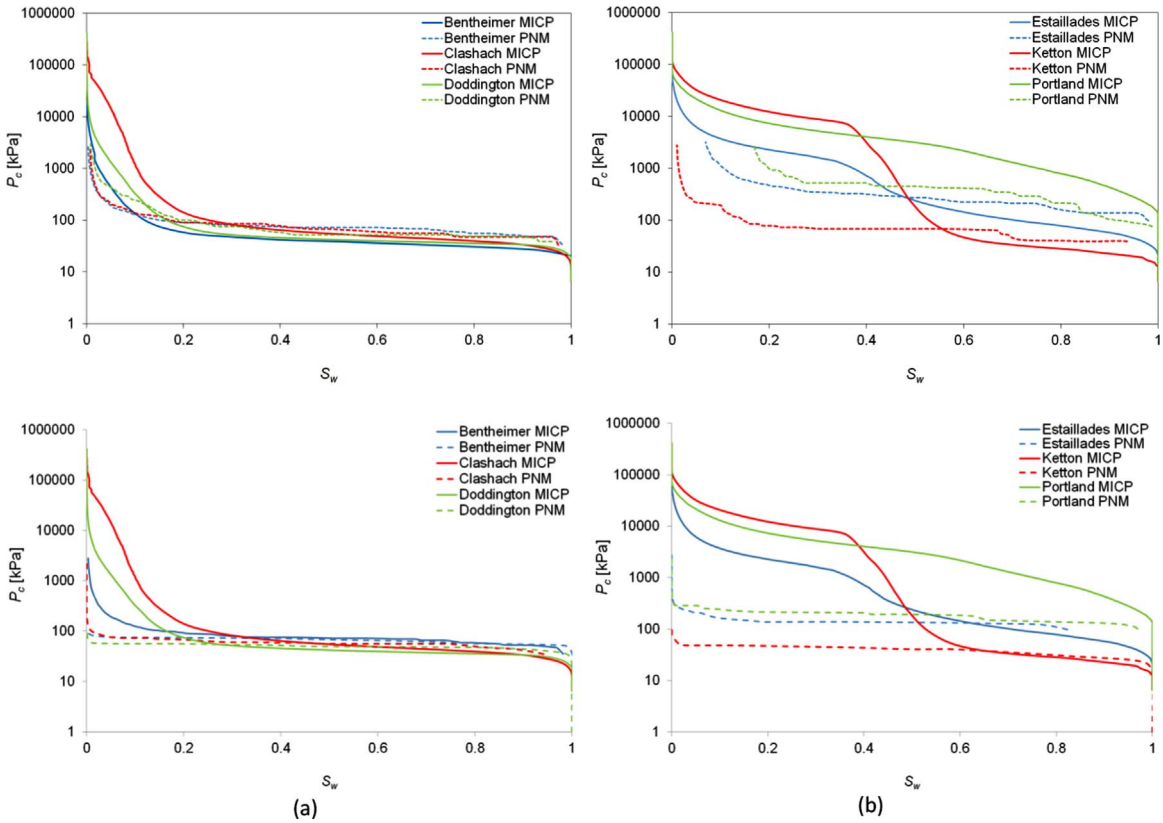

Fig. 9. Predicted and measured MICP for (a) the sandstone and (b) the limestone rocks. The top tiles are modelled with 512^3 subsets whereas the lower ones where using 1024^3.

512^3 subsets, this was also seen in the 1024^3 subsets for both PNM and lattice-Boltzmann methods. The 512 and 1024 subset image trend in permeability values was somewhat seen in the experimental values. Ketton has the highest experimental permeability which seems to be consistent with a visual inspection of a 2D slice of the tomogram (Fig. 3) this indicates that the large vuggy pores are well connected by resolvable smaller ones. This would be in agreement with the fact that the high experimental permeability is reproduced by image based modelling. We do note that the match is significantly better for the permeabilities compared to the porosities. This is most probably due to the unresolvable microporosity which will more significantly impact the porosity estimation. It is in line with this argumentation that the discrepancy is most pronounced fort the limestones where the unresolvable pore space is most explicit.

3.4. The image based capillary pressure curves

Fig. 9 shows the experimental and image-based capillary pressure curves. The modelling is based on mercury and air input parameters with a σ of 0.48 N/m and θ of 40°.

In the MICP experiments, the entire pore space is in principle accessible for displacement. This includes the clay and all of the porosity that is not fully resolvable by micro-CT imaging and analysis. Thus, the modelling goes all the way down to $S_w=0$. This necessarily means that the predictions at low S_w are poor because they involve unresolved pore space and this is observed. When the trend of the two data sets is compared it can be seen that the performance is the same for the saturations where there is agreement with experiment, that is the large plateau starting from roughly $S_w=0.2$ and ending at $S_w=1$. Below $S_w=0.2$ there is strong disagreement with the experimental values, for both subsets and variation in between the subsets too. Yet again, the reason for this can be attributed to the fact that the entire pore space is not fully resolved, a poor description of the small pores will lead to errors for the lower saturations. There is no particular improvement in increasing the subset size to 1024^3, if anything the 512^3 subset seems to provide the largest amount of details at the low saturations. For the limestone the situation is less obvious, but it seems that the capillary pressure curves are the most detailed for the small 512^3 subset. None of the image-based curves reproduce the slope around $S_w=0.5$, which is a common characteristic of a bimodal system. None of the image-based curves seem to resemble the experimental ones.

At high water saturation and low pressures the numerical predictions seem to be close to the measured values for sandstone rocks. This is an indication that the image-based analysis is capturing the large pores and throats of the sample quite well.

4. Conclusions

The results are best grouped into a survey of the sandstones and the limestone samples respectively. In this particular case, there does not seem to be enough evidence to say that a larger subset is always better. Use of the smaller subset will result in a decrease in computational demand especially for lattice-Boltzmann modelling. The agreement between image-based derived values and experimentally determined values is not very good. This comparison is independent of methodology and subset size. This lack of agreement can be attributed to insufficient resolution in the micro-CT experiment and the effect is most pronounced in the limestone case, where the experimental and imaged derived porosities differ by almost a factor of two. The disagreement between the experimental and image derived pore throat distribution functions is puzzling and could possibly be due to the method

of spanning the entire pore network volume. The permeability calculations and measurements are all within the same order of magnitude which is an indication unresolved issues in the way that the pore sizes are defined and converted into Pc data where the discrepancy between theory and experiment is quite significant. This is a potential topic for future analysis, as is cannot be attributed to limited resolution of the micro-CT image acquisition. That being said the first step towards achieving more predictive digital rocks methods will have to focus on the tomogram resolution with a possible focus on the micro porosity. This can be achieved in difference imaging experiments where tomograms of dry core are compared to tomograms of core filled with contrast agents. This will enable better description of the micro porosity which is a major caveat in estimating petrophysical parameters from CT images.

Acknowledgments

The authors would like to thank the Department of Earth Science and Engineering, Imperial College London for laboratory access and sharing the laboratory data.

References

Alizadeh, A.H., Piri, M., 2014. Three-phase flow in porous media: A review of experimental studies on relative permeability. Rev. Geophys. 52 (3), 468–521.
Alyafei, N., Gharbi, O., Raeini, A.Q., Yang, J., Iglauer, S., Blunt, M.J., 2013. Influence of micro-computed tomography image resolution on the predictions of petrophysical properties." In IPTC 2013: International Petroleum Technology Conference.
Alyafei, N., Raeini, A.Q., Paluszny, A., Blunt, M.J., 2015. A sensitivity study of the effect of image resolution on predicted petrophysical properties. Transp. Porous Media 110 (1), 157–169.
Andrew, M., Bijeljic, B., Blunt, M.J., 2014. Pore-scale imaging of trapped supercritical carbon dioxide in sandstones and carbonates. Int. J. Greenh. Gas. Control 22, 1–14.
Arns, C.H., Knackstedt, M.A., Pinczewski, W.V., Lindquist, W.B., 2001. Accurate estimation of transport properties from microtomographic images. Geophys. Res. Lett. 28 (17), 3361–3364.
Arns, C.H., Knackstedt, M.A., Pinczewski, W.V., Garboczi, E.J., 2002. Computation of linear elastic properties from microtomographic images: Methodology and agreement between theory and experiment. Geophysics 67 (5), 1396–1405.
Arns, C.H., Knackstedt, M.A., Pinczewski, W.V., Martys, N.S., 2004. Virtual permeametry on microtomographic images. J. Petro. Sci. Eng 45 (1–2), 41–46.
Bernaschi, M., Fatica, M., Melchionna, S., Succi, S., Kaxiras, E., 2010. A flexible high-performance Lattice Boltzmann GPU code for the simulations of fluid flows in complex geometries. Concurr. Comp. Pract. Exp. 22 (1), 1–14.
Biferale, L., Mantovani, F., Pivanti, M., Pozzati, F., Sbragaglia, M., Scagliarini, A., Schifano, S.F., Toschi, F., Tripiccione, R., 2013. An optimized D2Q37 Lattice Boltzmann code on GP-GPUs. Comput. Fluids 80, 55–62.
Blunt, M.J., Jackson, M.D., Piri, M., Valvatne, P.H., 2002. Detailed physics, predictive capabilities and macroscopic consequences for pore-network models of multiphase flow. Adv. Water Res. 25, 1069–1089.
Blunt, M.J., Bijeljic, B., Dong, H., Gharbi, O., Iglauer, S., Mostaghimi, P., Paluszny, A., Pentlan, C., 2012. Pore-scale imaging and modelling. Adv. Water Res. 51, 197–216.
Brenchley, P.J., Rawson P.F., 2006. The Geology of England and Wales. the Geological Society, London. (format and page).
Dong, H., Blunt, M.J., 2009. Pore-network extraction from micro-computerized-tomography images. Phys. Rev. E 80, 036307.
Dubelaar, C.W., Nijland, T.G., 2015. The Bentheim sandstone: Geology, petrophysics, varieties and its use as dimension stone. Eng. Geo. Soc. Territ. 8, 557–563.
Dullien, F.A.L., 1992. Porous Media: Fluid Transport and Pore Structure. Academic Press., New York.
Fenwick, D.H., Blunt, M.J., 1998. Three-dimensional modeling of three phase imbibition and drainage. Adv. Water Res. 21 (2), 121–143.
Jones, A.C., Arns, C.H., Hutmacher, D.W., Milthorpe, B.K., Sheppard, A.P., Knackstedt, M.A., 2009. The correlation of pore morphology, interconnectivity and physical properties of 3D ceramic scaffolds with bone ingrowth. Biomaterials 30 (7), 1440–1451.
Marquez, X., Fogden, A., McKay, T.J., Sølling, T.I., 2013. Multiscale characterization on the pore network in carbonates rocks, 166023-MS.
Ngwenya, B.T., Elphick, S.C., Shimmield, G.B., 1995. Reservoir sensitivity to water flooding: An experimental study of seawater Injection in a North Sea reservoir analog. AAPG Bull. 79 (2), 285–303.
Ribi, W., Senden, T.J., Sakellariou, A., Limaye, A., Zhang, S., 2008. Imaging honey bee brain anatomy with micro-X-ray-computed tomography. J. Neurosci. Methods 171 (1), 93–97.
Sakellariou, A., Arns, C.H., Sheppard, A.P., Sok, R.M., Averdunk, H., Limaye, A., Jones, A.C., Senden, T.J., Knackstedt, M.A., 2007. Developing a virtual materials laboratory. Materialstoday 10 (12), 44–51.
Santarelli, F.J., Brown, E.T., 1989. Failure of three sedimentary rocks in triaxial and hollow cylinder compression tests. Int. J. Rock. Mec. Min. Sci. Geomech. Abstr. 26 (5), 401–413.
Sheppard, A., Latham, S., Middleton, J., Kingston, A., Myers, G., Varslot, T., Fogden, A., Sawkins, T., Cruikshank, R., Saadatfar, M., Francois, N., Arns, C., Senden, T., 2014. Nuclear instruments and methods in physics. Res. Sect. B: Beam Interact. Mater. At. 324, 49–56.
Sok, R.M., Varslot, T., Ghous, A., Latham, S., Sheppard, A.P., Knackstedt, M.A., 2010. Pore Scale Characterization of Carbonates at Multiple Scales: Integration of Micro-CT, BSEM, and FIBSEM. Petrophysics 51 (6), 379–387.
Suicmez, V.S., Piri, M., Blunt, M.J., 2007. Pore-scale simulation of water alternate gas injection. Transp. Porous Media 66 (3), 259–286.
Turner, M.L., Knufing, L., Arns, C.H., Sakellariou, A., Senden, T.J., Sheppard, A.P., Sok, R.M., Limaye, A., Pinczewski, W.V., Knackstedt, M.A., 2004. Three-dimensional imaging of multiphase flow in porous media. Phys. A: Stat. Mech. Appl. 339 (1–2), 166–172.
Valvatne, P.H., Blunt, M.J., 2004. Predictive pore-scale modelling of two-phase flow in mixed wet media. Water Resour. Res. 40, W07406.
Watson, J., 1911. British and foreign building stones: A descriptive catalogue of the specimens in the Sedgwick museum. Univ. Press., Cambridge, UK.
Wildenschild, D., Sheppard, A.P., 2013. X-ray imaging and analysis techniques for quantifying pore-scale structure and processs in subsurface porous medium systems. Adv. Water Res. 51, 241–246.
Wilke, J., Pohl, T., Kowarschik, M., Rüde, U., 2003. Cache performance optimizations for parallel lattice Boltzmann codes, Euro-Par 2003 Parallel Processing, Proceedings. In: Kosch, H., Boszormenyi, L., Hellwagner, H. (Eds.), Book Series: Lecture Notes in Computer Science, p. 2790.